J. Fluid Mech. (2016), *vol.* 808, *pp.* 224–244.
doi:10.1017/jfm.2016.643

Crossflow instability in a hypersonic boundary layer

Stuart A. Craig[1,2,†] **and William S. Saric**[2]

[1]Department of Aerospace & Mechanical Engineering, University of Arizona, Tucson, AZ 85721, USA

[2]Department of Aerospace Engineering, Texas A&M University, College Station, TX 77843, USA

(Received 28 January 2016; revised 11 August 2016; accepted 2 October 2016;
first published online 27 October 2016)

The crossflow instability in a hypersonic, laminar boundary layer is investigated using point measurements inside the boundary layer for the first time. Experiments are performed on a 7° right, circular cone with an adiabatic wall condition at 5.6° angle of incidence in the low-disturbance Mach 6 Quiet Tunnel at Texas A&M University. Measurements are made with a constant-temperature hot-wire anemometer system with a frequency response up to 180 kHz. Stationary crossflow waves are observed to grow and saturate. A travelling wave coexists with the stationary wave and occurs in a frequency band centred around 35 kHz. A type-I secondary instability is also observed in a frequency band centred around 110 kHz. The behaviour of all three modes is largely consistent with their low-speed counterparts prior to saturation of the stationary wave. Afterward, the behaviour remains in partial agreement with the low-speed case. Neither type-II secondary instability nor transition to turbulence are observed in this study.

Key words: boundary layer stability, compressible boundary layers, transition to turbulence

1. Introduction

The design of hypersonic vehicles is beset by a number of important challenges, chief among them the accurate prediction of aerodynamic heating and efficient operation of scramjet engines where applicable. Each of these challenges is closely related to the challenge of boundary-layer stability and transition, as a turbulent boundary layer implies a higher surface heat transfer rate and improved inlet performance and fuel–air mixing in the engine. Of lesser, but still significant importance is the effect of transition on viscous drag.

Crossflow arises on a number of geometries found ubiquitously on hypersonic vehicles such as swept surfaces, axisymmetric bodies at non-zero angle of incidence or rotating axisymmetric bodies. The body geometry combined with the pressure gradient results in curved inviscid streamlines at the boundary-layer edge, where the stream-normal component of the pressure gradient serves as the centripetal force. Near the wall, the velocity is reduced but the pressure gradient is constant, resulting in a non-zero-velocity component normal to the inviscid streamlines called crossflow.

† Email address for correspondence: sacraig@email.arizona.edu

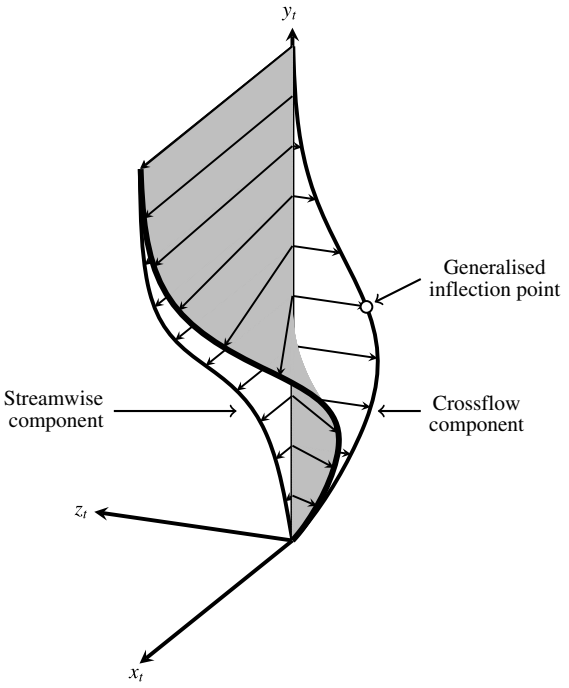

FIGURE 1. A typical crossflow profile calculated from a compressible Falkner–Skan–Cooke solution. Profiles are of the streamwise and crossflow components of mass flux (ρU and ρW respectively) and their sum. The generalised inflection point is the compressible counterpart to Rayleigh's criterion in subsonic flows (Mack 1984) and represents $D(\rho DW) = 0$, where $D = \mathrm{d}/\mathrm{d}y$.

A typical crossflow profile is depicted in figure 1. The crossflow profile necessarily includes an inflection point and is therefore a source of inviscid instability (Saric, Reed & White 2003).

The crossflow instability manifests in the boundary layer as a wave oriented in the crossflow direction. While both the stationary and travelling varieties of these waves may be unstable, their initial amplitudes are determined independently by surface roughness and the free-stream turbulence level, respectively. As a result, while travelling waves are typically more unstable, it is often the stationary wave that dominates the transition process in low-disturbance environments such as in flight (Deyhle & Bippes 1996).

The stationary wave produces very weak $(\rho v)'$ and $(\rho w)'$ disturbances. However, since the wavenumber vector is nearly orthogonal to the inviscid streamlines, the integrated effect of these disturbances is to convect $O(1)$ momentum into the boundary layer, producing substantial mean-flow modification. This results in a modified basic state and a rapid breakdown of linear theory. Stationary crossflow has been the subject of considerable study in low-speed flows. The early history of crossflow research is reviewed in Reed & Saric (1989) and more recent reviews are given by Bippes (1999) and Saric *et al.* (2003).

In these low-speed studies, transition does not occur due to the primary wave itself. Instead, the mean-flow distortion serves to stabilize the stationary wave and causes saturation to occur. Transition then occurs downstream of the saturation

point, often after a considerable distance. Kohama (1987) first suggested that the breakdown was a result of a class of inflectional secondary instabilities that develop in the modified mean flow, supporting evidence for which was first provided by Kohama, Saric & Hoos (1991). The various secondary instability modes that were subsequently discovered have been classified by Malik, Li & Chang (1996) into two broad categories: type-I modes produced by spanwise or azimuthal gradients of the streamwise mean flow ($\partial U/\partial z$ or $\partial U/\partial \theta$), and type-II modes produced by the wall-normal gradients ($\partial U/\partial y$ or $\partial U/\partial r$). These mechanisms have been studied extensively at low speeds, for example by Malik *et al.* (1999), Wassermann & Kloker (2002), White & Saric (2005) and Bonfigli & Kloker (2007).

While crossflow has been studied extensively at low speeds, it has received little attention in hypersonic boundary layers despite the ubiquity of the relevant flow geometries in hypersonic vehicle designs. Early experiments focused on features such as the vortex pattern (Adams 1971) and transition location as a function of angle of attack and nose bluntness (Stetson 1982), but did not address the finer details of the boundary layer. More recent wind-tunnel experiments have taken more care to study the boundary-layer physics. However, these experiments have largely been confined to impulse facilities, where run times limit the practicality of many off-body measurement techniques. Focused laser differential interferometry (FLDI) has been employed to study Mack-mode instability waves (Parziale, Shepherd & Hornung 2013, 2015), but the relatively large depth of field limits its applicability to flows with small three-dimensional structures such as crossflow. Hot-wires have also been employed (cf. Schmisseur, Young & Schneider 1996), but are only capable of one measurement location per tunnel run and suffer from durability issues. Consequently, crossflow experiments performed in impulse facilities have been largely limited to surface measurements such as pressure, temperature and heat flux (cf. van den Kroonenberg *et al.* 2010; Swanson & Schneider 2010; Muñoz, Heitmann & Radespiel 2014; Ward, Henderson & Schneider 2015).

Recently, flight tests have been performed on a hypersonic, crossflow-dominated, elliptic cone (Dolvin 2008). The elliptic forebody of the test article was dedicated primarily to transition research and featured accompanying computational (Choudhari *et al.* 2009; Li *et al.* 2012; Gosse, Kimmel & Johnson 2014) and wind-tunnel experiments (Borg, Kimmel & Stanfield 2015; Juliano, Borg & Schneider 2015). While it was the largest hypersonic crossflow study to date, this program was unable to provide detailed boundary-layer measurements due to the limitations of flight testing and the Ludwieg tube in which the wind-tunnel experiments were performed. Further, the choice of an elliptic cone was made to approximate the shape of a hypersonic glide vehicle subject to both the crossflow and Mack-mode instabilities (Mack 1984) rather than to isolate crossflow.

In order to isolate super- and hypersonic crossflow for study, a standard geometry conducive to both experiments and computation has been adopted: a right, circular cone with a semivertex angle of 7° and typically placed at 6° angle of incidence to the flow. This geometry was the subject of an study by Schuele, Corke & Matlis (2013) wherein the effects of azimuthally periodic discrete roughness elements (DREs) on the crossflow instability at Mach 3.5 were studied with Pitot measurements in the boundary layer. It has also been studied computationally by Balakumar (2009).

This geometry has also been the subject of considerable computational study at Mach 6. Balakumar & Owens (2010) performed a direct numerical simulation (DNS) on a cone with both a smooth wall and with two patterns of DREs. Kuehl, Perez & Reed (2012) and Perez, Reed & Kuehl (2013) have performed stability analyses using

the parabolized stability equations, culminating in a new code based on the nonlinear parabolized stability equations (NPSE) for hypersonic stability analysis (Oliviero *et al.* 2015). This code was used in conjunction with linear stability theory and a spatial biglobal analysis by Moyes *et al.* (2016), who matched their geometry and conditions with those of the present work. Additionally, Gronvall, Johnson & Candler (2012) performed a DNS with distributed roughness placed near the tip along the attachment line. However, no detailed boundary-layer measurements have yet been performed to accompany these computational studies.

The lack of detailed experimental data has forced such computational studies to rely only on surface measurements for validation. The objective of this study is therefore twofold: to provide the first experimental study of the physics of hypersonic crossflow featuring detailed off-body measurements in the boundary layer, and to provide a more comprehensive set of validation data including details of the structure of the boundary layer. Particular attention is given to the details of both the primary and secondary instabilities and their similarities with low-speed flows. To this end, the experimental apparatus and method are detailed in § 2, the details of the stationary wave are presented in § 3.1, the details of the fluctuation data are given in § 3.2, comments on the effects of free-stream disturbances are given in § 3.3 and conclusions are made in § 4.

2. Experimental apparatus and method

2.1. *Wind tunnel*

Experiments were performed in the Mach 6 Quiet Tunnel (M6QT) at Texas A&M University (TAMU). This facility was the result of an effort to design quiet, hypersonic facilities at NASA Langley Research Center spanning several decades and culminating in the 1990s with the M6QT (Chen, Wilkinson & Beckwith 1993; Blanchard, Lachowicz & Wilkinson 1997). The settling chamber and nozzle were then transferred to TAMU in 2005 where they were refurbished (including repolishing the nozzle) and integrated into the infrastructure at the National Aerothermochemistry Laboratory (NAL). Initial flow quality testing (Hofferth, Bowersox & Saric 2010) showed that tunnel performance was consistent with Blanchard *et al.* with free-stream fluctuation levels of $p'_{t2,rms}/p_{t2} \leqslant 0.05\,\%$ in the quiet core.

In its present configuration at TAMU, M6QT is a pressure–vacuum blowdown tunnel with approximately 40 s of constant-condition run time. The facility is capable of quiet operation in the range $4.6 \times 10^6\ \mathrm{m}^{-1} \leqslant Re' \leqslant 11.0 \times 10^6\ \mathrm{m}^{-1}$, corresponding to a settling chamber pressure of approximately 400 kPa $\leqslant p_{t1} \leqslant$ 950 kPa. Prior to each run, the tunnel is convectively preheated to avoid oxygen liquefaction in the test section as well as provide a more stable total temperature while data are collected. For each data set in the present experiments, the tunnel is operated at $p_{t1} = 900$ kPa, $T_t = 430$ K, and $Re' = 10.0 \times 10^6\ \mathrm{m}^{-1}$. Infrared thermography is additionally reported at $Re' = 11.0 \times 10^6\ \mathrm{m}^{-1}$.

2.2. *Cone model and alignment*

The present experiment utilizes the standardised geometry of a right circular cone with a semivertex angle of 7° (figure 2). The model is placed in the tunnel at 5.6° of yaw (this angle is used instead of the typical 6° to minimize tunnel blockage and ensure reliable tunnel operation). It is constructed entirely of 17-4 PH stainless steel and is 430 mm in length from the nominal tip to the base. The removable sharp tip measures

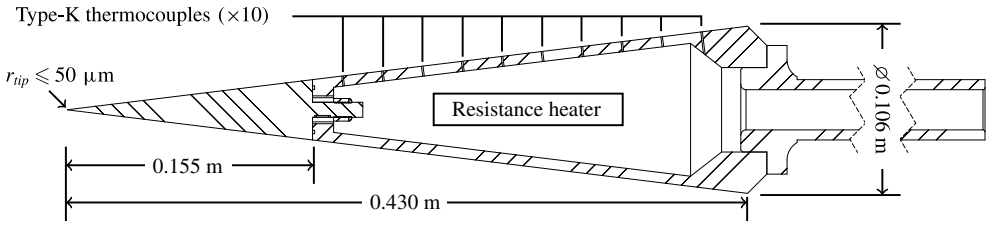

FIGURE 2. Schematic of the 7° cone model. The resistance heater is operated with a proportional-integral-derivative (PID) controller using the mean value of the thermocouple measurements.

155 mm in length with a tip radius of $r_{tip} \leqslant 50$ μm and includes an O-ring at its interface with the frustum to prevent any mass flow through the gap. The root-mean-square (r.m.s.) surface roughness is $R_q \approx 2.15$ μm.

Changes in wall temperature ratio, T_w/T_{aw}, do not affect the fundamental mechanism driving the crossflow instability; however, secondary instabilities are convective in nature and their frequencies are expected to scale with boundary-layer thickness, δ. Since δ is affected by T_w/T_{aw}, it is therefore important that T_w/T_{aw} be held as constant as possible over the course of each run and over the course of each run comprising the data set. This is most readily achieved by enforcing an adiabatic wall condition, $T_w/T_{aw} = 1$. To this end, the frustum is hollow and features thick walls to minimize the temperature change during a run. An array of ten equally spaced type-K thermocouples is embedded in the surface along a ray. The mean of these temperature measurements is used by a PID-controlled resistance heater to warm the model to just below T_{aw} prior to each run. During the preheat, the temperature of the model is raised slightly until $T_w/T_{aw} \approx 1$ throughout the course of the tunnel run. During a typical run, an individual thermocouple varies by $\Delta T < 1$ K. The thermocouples nearest the tip and base generally report a slightly lower temperature due to the large thermal mass in those regions. Near the tip, $T_w/T_{aw} \approx 0.99$ and near the base, $T_w/T_{aw} \approx 0.96$. In the present study, the aft-most measurement location is at $T_w/T_{aw} \approx 0.99$.

Vertical alignment was achieved utilizing a focusing schlieren deflectometer (FSD) detailed in Hofferth *et al.* (2013). The model was placed in the flow at nominally 0° angle of incidence and the pitch was adjusted until the FSD indicated that the instability waves on the top and bottom of the model exhibited equal frequencies. Equal frequencies indicated that the flow was symmetric relative to the horizontal plane and the model was at 0° pitch. The entire mounting system is designed with a pivot to allow adjustable yaw, and was placed at 5.6° using a confocal laser displacement sensor in a manner similar to Hofferth & Saric (2012). In the present study, the laser was used to locate the exit plane of the nozzle while being held at a constant z-location relative to the model using the traverse detailed in § 2.4.

The cone was placed into the nozzle such that all but approximately 50 mm near the base were fully inside the nozzle exit plane. At the operating pressures used in this study, this means that the region of higher tunnel noise intersects the model when installed axisymmetrically at approximately $z = 280$ mm. However, as the model is installed at a non-zero angle of incidence, the actual intersection point will be further forward on the windward side and further aft on the leeward side. A diagram of the model superimposed over the free-stream pressure fluctuation field from Hofferth & Saric (2012) is depicted in figure 3. It is not expected that this noise meaningfully affects the results of this study. This shall be discussed further in § 3.3.

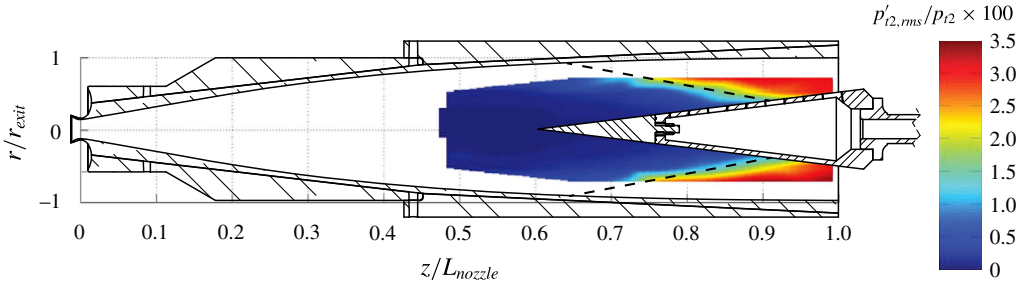

FIGURE 3. (Colour online) The cone model superimposed over a contour of the free-stream total pressure fluctuations at $Re' = 10 \times 10^6$ m^{-1}. Black dashed lines indicate approximate onset of higher free-stream pressure fluctuations.

2.3. *Measurement technique*

Of principal interest to this study are point measurements of the mass flux and its high-frequency fluctuations about the mean. Constant-temperature hot-wire anemometry (CTA) is therefore the instrument of choice for the present experiment. The hot-wire probes were manufactured in-house at NAL by the author and utilized Wollaston wire composed of 90 %/10 % platinum–rhodium with a diameter of 5 μm for the sensing element. The active length, ℓ, of the wires was typically between 600 μm and 700 μm, resulting in $120 \leqslant \ell/d \leqslant 140$. The upper limit of ℓ corresponds to approximately 0.15 times the smallest observed stationary crossflow wavelength and is approximately equal to the step size in the azimuthal direction. The probes were operated at a high temperature loading factor ($\tau \approx 0.8$) such that they were primarily sensitive to mass flux (Smits, Hayakawa & Muck 1983; Semper 2013).

Hot-wire probes were tuned *in situ* at the location of maximum fluctuations in the boundary layer. The input pulse and wire response are both recorded using a computer-based oscilloscope and the frequency-response function is calculated. Probes reliably achieved a frequency response of approximately 180 kHz at their −3 dB rolloff point.

While the wire voltage remains uncalibrated in the present study, a pseudo-calibration method was employed in order to map each voltage approximately to mass flux normalized by its edge value. Classically, a hot-wire may be calibrated to mass flux based on King's law,

$$E^2 = L + M(\rho u)^n, \tag{2.1}$$

where E is the hot-wire voltage, ρu is the mass flux and L and M are calibration constants. For sufficiently high wire-diameter Reynolds number, Re_d, $n \approx 0.55$. However, at the conditions of the present experiment, $Re_d = O(1)$ and the typical value no longer holds. Several experiments using a CTA with a similar wire at similar conditions to those in M6QT (Semper 2013), as well as a preliminary calibration performed in another set of experiments in M6QT (Hofferth & Saric 2012; Hofferth 2013) have shown $n \approx 1$ across the operating range of those facilities. E^2 is therefore approximately linear in ρU. In light of this, each set of data points taken during a single run is accompanied by a pair of normalization values: one near the wall (E_w^2) and one just outside the boundary layer (E_e^2). In this manner, the squared hot-wire

voltage at any given point in the boundary layer (E^2) is calibrated to the normalized mass flux as

$$\frac{E^2 - E_w^2}{E_e^2 - E_w^2} \approx \frac{\rho^* u^*}{\rho_e^* u_e^*} = \rho u, \tag{2.2}$$

as the constants L and M fall out in the normalization. Here, stars indicate dimensional quantities and, henceforth, the normalized mass flux defined in (2.2) shall be referred to simply as ρu.

The primary source of uncertainty in this calibration method arises from the uncertainty in the wall location. Since the probe cannot be placed exactly on the wall, the wall point was acquired approximately 0.5 mm $\pm$ 0.1 mm above it. This results in up to 10 % error in the normalized ρu measurement, with the effect being more dramatic near the wall and tending toward zero as the distance from the wall increases.

2.4. *Motion control and data acquisition*

Hot-wire probes are positioned using a special three-dimensional probe-traversing mechanism that was designed and built for this experiment. This system operates in cylindrical coordinates and is affixed coaxially to the model. This configuration allows all measurements to be made in a model-oriented coordinate system regardless of the angle of incidence to the flow or the test section. The model coordinate system is defined cylindrically as (r, θ, z) with $\boldsymbol{v} = (u_r, u_\theta, u_z)$ and r normal to the axis of the model. In the present study, $r = 0$ is always defined at the wall at a given z location, $\theta = 0$ is defined at the windward attachment line, and $z = 0$ is defined as the tip. All data are acquired in planes of constant z.

The aforementioned ± 0.1 mm uncertainty applies to the wall-normal (r) position. On a run-to-run basis, the actual error in wall-normal position is identical so long as the probe has not been removed between runs. As a result, the wall-normal positioning error is identical among the runs conducted at $z = 360$, 370, and 380 mm, as well as those conducted at $z = 350$ mm and 390 mm.

We next introduce a wall-normal coordinate system (x_n, y_n, z_n) with corresponding velocities (u_n, v_n, w_n) such that x_n runs parallel to the model wall at constant θ and y_n is normal to the wall. The hot-wire probes are oriented such that they lie in the (x_n, y_n) plane with the axis of the wire oriented along z_n. The wire is nearly insensitive to ρw_n along its axis and therefore measures $(\rho u_n, \rho v_n)$. Due to the angle of incidence, the inviscid streamlines are curved and cross the hot-wire probe at a non-zero angle. Since stability calculations are often performed in coordinate systems aligned with the inviscid streamlines, $\boldsymbol{v}_t = (u_t, v_t, w_t)$, it should be noted that the measurements performed here are a projection of $\boldsymbol{v}_t$ onto the (x_n, y_n) plane. All hot-wire data presented herein are the magnitude of $(\rho u_n, \rho v_n)$ in planes of constant z (in the cylindrical, model-fixed coordinate system).

Owing to the finite length of each tunnel run, each plane of data is acquired over the course of multiple runs. Run-to-run variability was typically less than 1 % of the measured CTA voltage. During a typical 30-second run, the hot-wire probe begins outside of the flow at $\theta = 0$ to protect it from the starting shock. It then moves into position at $\theta = 112°$ during the first 10 s of the run. Data are collected at 24 points at constant (r, z) and the wire is moved into position behind the cone to protect it from the unstart of the tunnel. This process is repeated many times until a suitable range in r has been covered to capture the boundary layer. Typically, the spacing in r is

100–200 μm, providing 13–31 vertical points in the boundary layer, and the spacing in θ is 0.5°, providing 25 points spanning approximately two crossflow wavelengths.

Data were sampled with 16 bits of resolution at 1 MHz. The signal was passed through a 500 kHz analogue, low-pass anti-aliasing filter prior to sampling. The signal-to-noise ratio was typically approximately 50 dB. The signal was separately passed through an AC-coupled amplifier with a 1 kHz high-pass filter in order to fill the voltage range of the data acquisition system for measurement of the fluctuations.

2.5. *Infrared thermography*

Complementary flow visualisation was performed using infrared (IR) thermography. The tunnel was fitted with an IR-transparent window and a FLIR SC8100 IR camera was used to record a section of the cone during a run. In order to enable IR thermography on the reflective steel model, a region near the base of the cone was covered with black, fiberglass-reinforced, PTFE-coated tape. Including the adhesive, this tape measured 175 μm in thickness. The low thermal conductivity of the tape allows a temperature gradient to exist on the surface and the differential heating typical of crossflow vortices is visible on the non-reflective surface in IR. The patch covers the region 380 mm $\leqslant z \leqslant$ 430 mm and 112.5° $\leqslant \theta \leqslant$ 247.5°, where $\theta = 180°$ is the leeward attachment line.

Due to the possibility of the tape interfering with the flow, no CTA measurements were performed in regions under its influence.

3. Results

3.1. *Mean flow*

IR flow visualisation was performed at two tunnel operating conditions (figure 4). $Re' = 10.0 \times 10^6$ m^{-1} corresponds to the run condition used for the CTA data in the present study. As is evident in figure 4(*a*), the canonical streak heating pattern as a result of the azimuthally varying shear in a crossflow boundary layer is visible over much of the area of the patch. The streaks remain clearly visible and distinct all the way to the base of the model except near the attachment line where the flow is not dominated by classical crossflow vortices (see Balakumar & Owens 2010). It is clear from this image that transition to turbulence does not occur, even at the base of the model, in any crossflow-dominated region.

The second run condition visualised was $Re' = 11.0 \times 10^6$ m^{-1}. This condition corresponds to the maximum Re' achievable under quiet flow conditions, albeit with some intermittency. The right image in figure 4 depicts this case and features the same streak pattern shown at the lower Re'. Again, the streaks persist to the base of the cone, and transition does not occur. As a result, it is expected that turbulent transition is not achievable on this model under quiet conditions in M6QT without forcing.

The streak patterns shown in figure 4 were repeatable from run to run for a given installation of the model, indicating that the vortices are likely body fixed.

CTA data were acquired at five z locations: $z = 350$, 360, 370, 380 and 390 mm. These locations correspond to $Re_z = 3.5 \times 10^6$, 3.6×10^6, 3.7×10^6, 3.8×10^6 and 3.9×10^6 respectively (where Re_z is defined using free-stream conditions and z is measured along the axis of the model). Mean-flow contours were constructed using the time-averaged mass flux, $\overline{\rho u}$, at each point. Mode shapes were generated by taking the azimuthal average of the mean mass flux and subtracting it from the mean-flow values

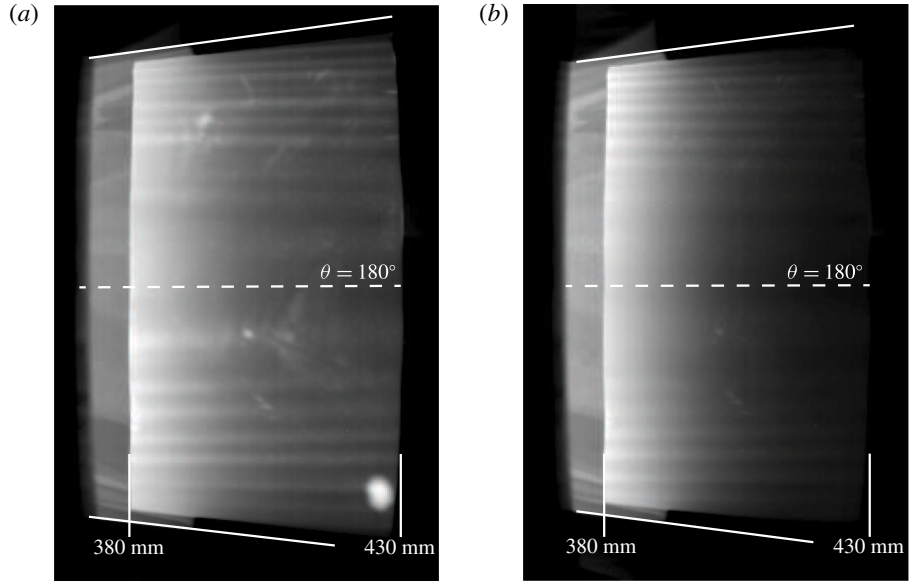

FIGURE 4. IR thermography depicting the hallmark heating pattern of crossflow vortices at the base of the cone at two run conditions. Solid white lines depict the top and bottom edges of the model. Flow is left to right. (*a*) $Re' = 10.0 \times 10^6$ m^{-1}, (*b*) $Re' = 11.0 \times 10^6$ m^{-1}.

at each height, then taking the azimuthal r.m.s. of the resulting mean disturbance profile, or $\left(\overline{\rho U} - \left\langle \overline{\rho U} \right\rangle_\theta\right)_{rms}$ at each r. Figure 5 depicts contours of the mean flow at each Re_z (*a*,*c*,*e*,*g*,*i*) with their corresponding mode shapes (*b*,*d*,*f*,*h*,*j*).

Immediately obvious from the figure is that even at $Re_z = 3.5 \times 10^6$, the most upstream location, the stationary wave has grown to 20.7 % amplitude. While it does not yet exhibit the characteristic rollover of crossflow vortices, it does appear that this behaviour is already imminent. The dominant circumferential wavenumber falls into the range $50 \leqslant k_c \leqslant 60$ ($6° \leqslant \lambda_c \leqslant 7.2°$), in agreement with linear calculations performed by Kuehl *et al.* (2012). Here, k_c is the wavenumber per circumference, λ_c is the circumferential wavelength, and $k_c = 360°/\lambda_c$.

One step downstream, at $Re_z = 3.6 \times 10^6$, the degree of development of the stationary vortex structure has visually regressed toward a more sinusoidal state. However, the mode shape indicates that the wave is still growing, with a maximum amplitude of 22.1 %. Additionally, the mode shape itself has become more irregular, showing evidence of the development of a secondary maximum beneath the existing maximum. Indeed, at $Re_z = 3.7 \times 10^6$, the vortices now exhibit the classical rollover structure and a very clear secondary maximum has developed in the stationary mode, which now reaches a maximum amplitude of 22.8 %.

The remaining two measurement locations exhibit a gradual degradation of the stationary vortex structure. The troughs between each upwelling have begun to fill in with lower-momentum fluid and the magnitude of $\nabla(\overline{\rho u})$ has started to decrease, as indicated by the spacing between the 10 % contour lines. The mode shapes show a corresponding decrease in amplitude and the two maxima have become less distinct in each case. The amplitudes at $Re_z = 3.8 \times 10^6$ and 3.9×10^6 are 18.6 % and 17.6 % respectively.

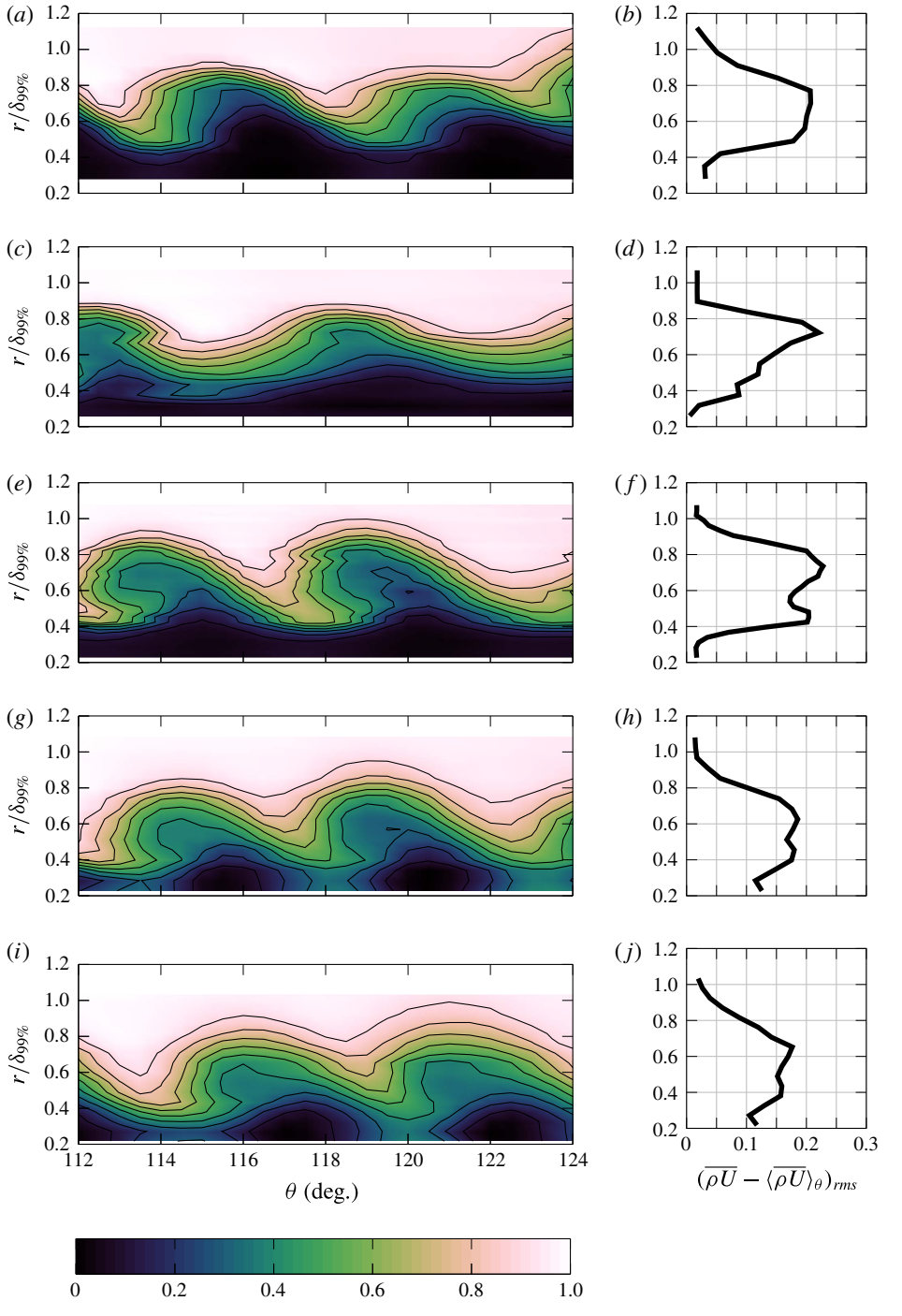

FIGURE 5. (Colour online) Mean-flow contours (*a*,*c*,*e*,*g*,*i*) and their associated stationary-mode shapes (*b*,*d*,*f*,*h*,*j*) for each measurement location. Colour contours are of $\overline{\rho u}$ as per (2.2). Line contours are increments of 10 % of the mean flow. Starting from the top, the locations are: $Re_z = 3.5 \times 10^6$, 3.6×10^6, 3.7×10^6, 3.8×10^6 and 3.9×10^6.

It is therefore evident that by the middle measurement location, the stationary crossflow wave has reached a state of nonlinear saturation and subsequently begins to attenuate. Additionally, the appearance of the secondary maximum in the mode amplitude tracks very closely with the development of saturation. Both of these phenomena (nonlinear saturation and a secondary maximum in the mode shape) have been observed in incompressible flows, including experiments performed at speeds as low as $M \approx 0.1$ (Saric *et al.* 2003; White & Saric 2005). Notably different in the Mach 6 case, however, is that the secondary peak in the mode shape occurs below the primary peak.

3.2. *Fluctuations*

The fluctuating component of ρu was also analysed by band-passing the hot-wire signal at 300 Hz and 180 kHz in order to remove content below the cutoff of the pre-amplifier and above the frequency response of the hot-wire probe respectively. Figure 6 depicts contours of the r.m.s. of the fluctuations in time at each measurement location. It is evident that, at each location, the regions of maximum fluctuation levels coincide with regions of high $|\nabla(\rho u)|$. The r.m.s. fluctuation level is abnormally high in the most upstream location at 11.6 %, before settling down at the last four locations where it measures 7.2 %, 7.8 %, 8.1 % and 7.8 % respectively. The reason for the large fluctuations at $Re_z = 3.5 \times 10^6$ before settling to a lower, nearly steady level is unclear at present.

It is clear that the shape of the fluctuating bands in figure 6 are evolving in space. It is therefore useful to investigate the spectral composition of the fluctuations and look for frequency bands that exhibit a high degree of spatial coherence. To this end, power spectra of each point were calculated using Welch's method (Welch 1967) with a Hanning window of size 1024 and a 50 % window overlap. The spectra were then placed in a three-dimensional array, $\mathcal{P}_{ijk}$, where the i dimension corresponds to r, the j dimension to θ and the k dimension to f from the Fourier analysis. In this way, each slice of $\mathcal{P}$ at constant k represents a contour in the (r, θ) plane of the frequency content at frequency f_k. From this analysis, two frequency bands were identified with their energy concentrated in relatively small and specific regions in space: 15 kHz $\leqslant f \leqslant$ 60 kHz, denoted [15, 60], and 80 kHz $\leqslant f \leqslant$ 130 kHz, denoted [80, 130]. Fluctuations outside of these bands tended to be nearly evenly distributed throughout the measurement region.

The ρu signal at each point was run through an 8-pole Butterworth digital band-pass filter for each of the bands of interest. Figure 7 depicts contours of the r.m.s. fluctuations in the [15, 60] band. Energy in this band is located in the high-gradient areas between each upwelling and grows more concentrated as the flow develops.

This frequency band approximately coincides with one observed by Muñoz *et al.* (2014) on nearly identical geometry using surface pressure measurements. In their study, Muñoz *et al.* attributed the energy in this band to the presence of first-mode waves growing concurrently with the stationary crossflow wave. However, computations by Kuehl *et al.* (2012) suggest that the most unstable travelling crossflow waves at the present measurement locations fall into this frequency band for $k_c = 42$. A set of follow-up calculations performed by Oliviero *et al.* (2015) utilizing NPSE at the $Re_z = 3.7 \times 10^6$ location on the present geometry show a broad region of highly amplified travelling crossflow in the same frequency and wavenumber bands observed in the present experiments (figure 8). It is therefore apparent that travelling crossflow waves are the more likely source of the energy in the [15, 60] band.

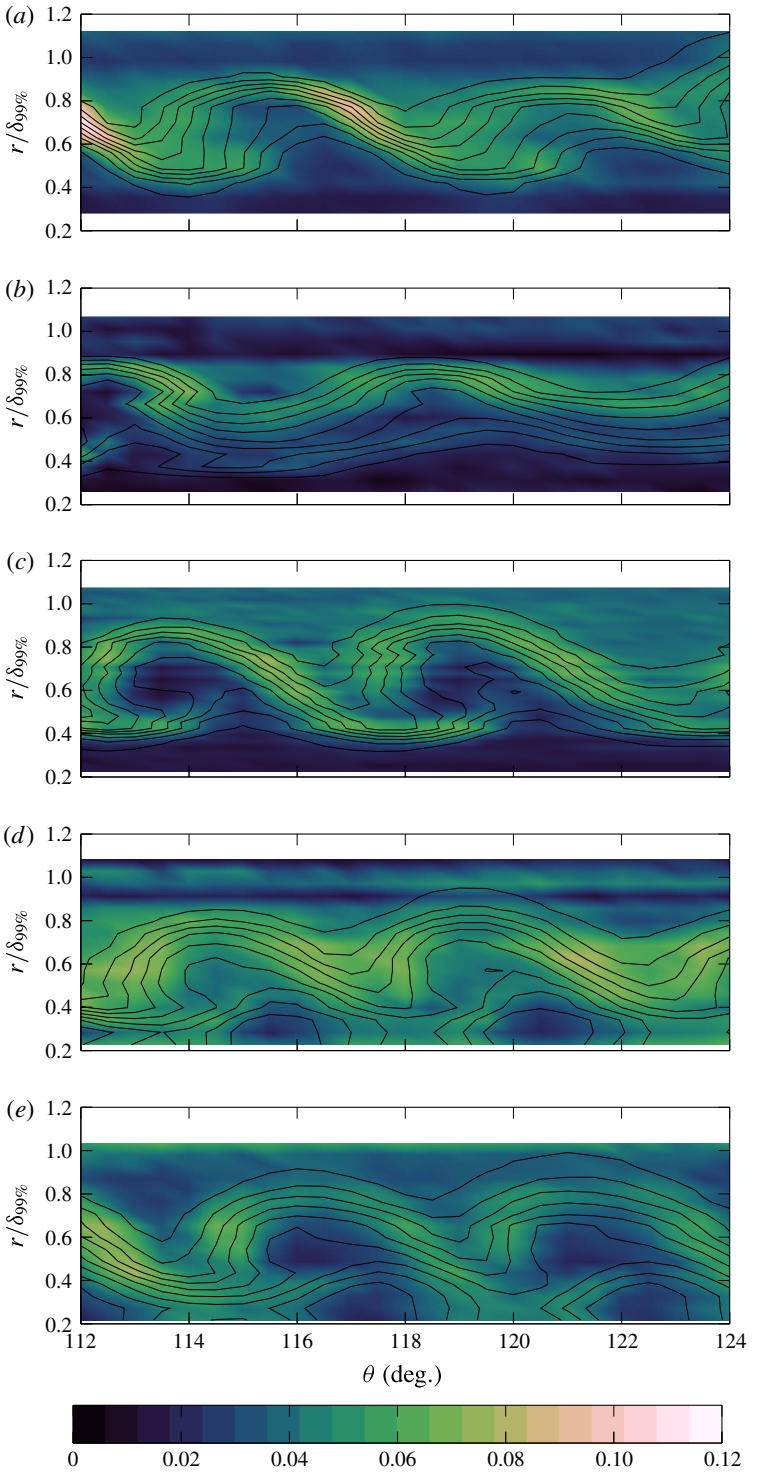

FIGURE 6. (Colour online) Colour contours of r.m.s. fluctuations with line contours of 10 % mean flow overlaid. Colour contours are of $(\rho u)_{rms}$. Starting from the top, the locations are: $Re_z = 3.5 \times 10^6$, 3.6×10^6, 3.7×10^6, 3.8×10^6 and 3.9×10^6.

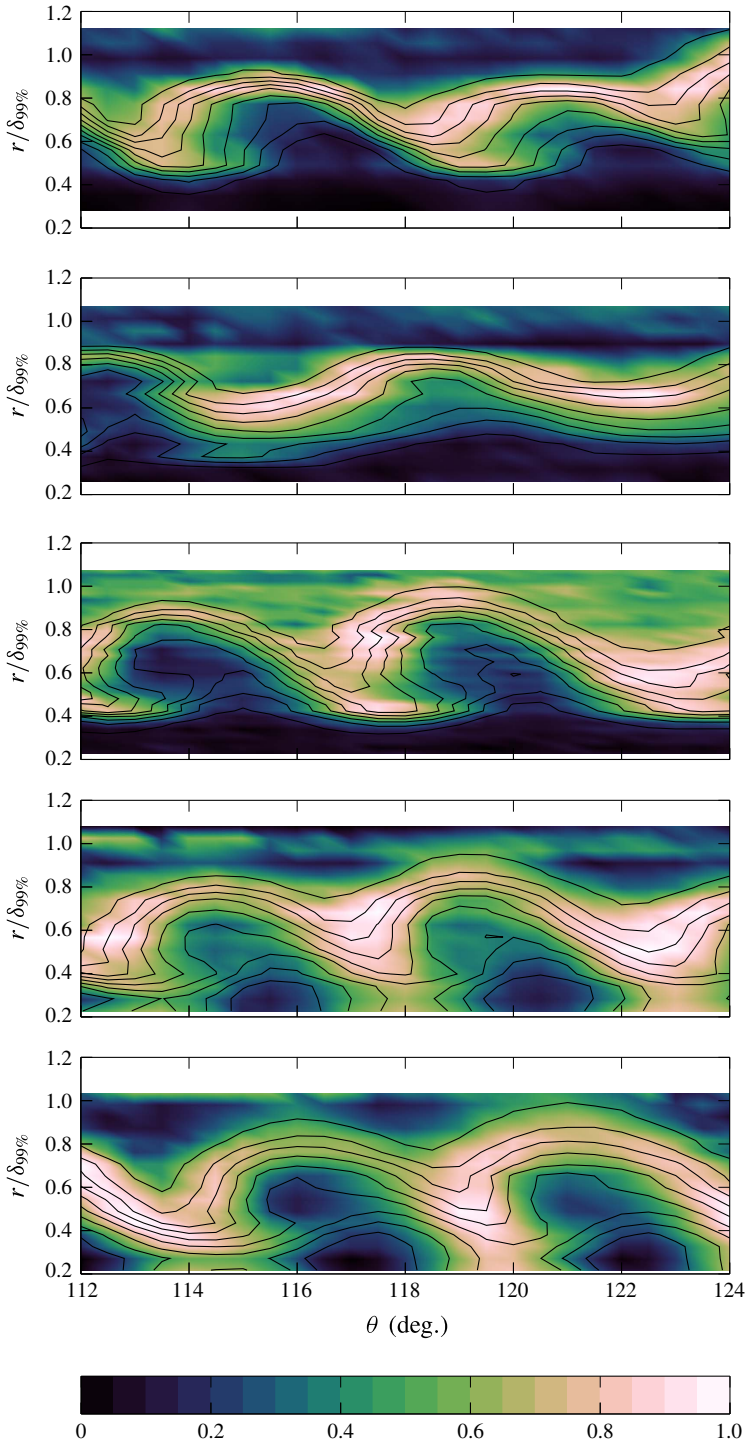

FIGURE 7. (Colour online) Contours of r.m.s. fluctuations in the [15, 60] band. Contour values are of the r.m.s. of the filtered signal normalized by the maximum filtered r.m.s. measured across all measurement stations. Starting from the top, the locations are: $Re_z = 3.5 \times 10^6$, 3.6×10^6, 3.7×10^6, 3.8×10^6 and 3.9×10^6.

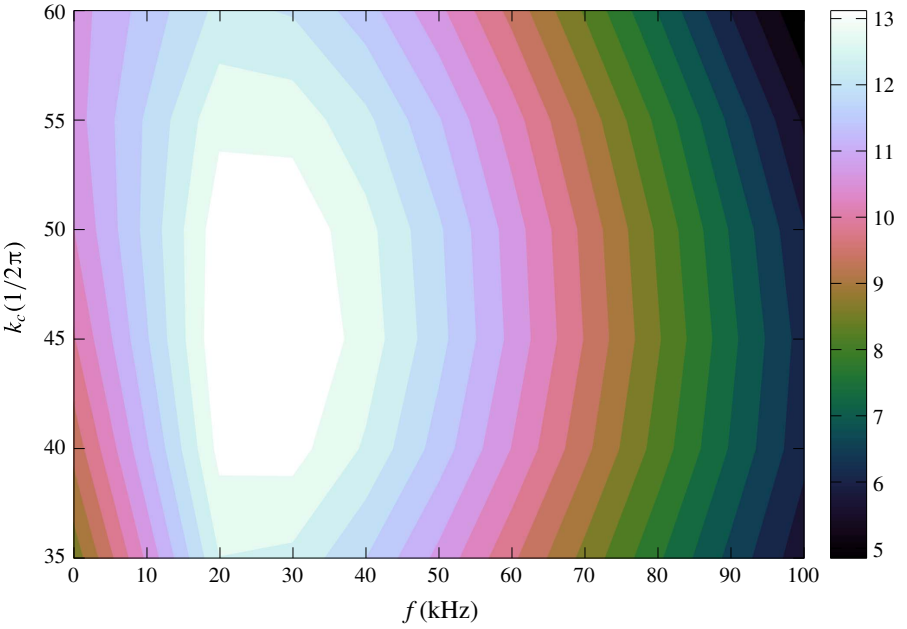

FIGURE 8. (Colour online) N-factor contour for travelling waves at $Re_z = 3.7 \times 10^6$ calculated using NPSE.

These travelling waves also share some of their behaviour with the travelling crossflow waves observed in low-speed flows (White & Saric 2005). In those experiments, travelling crossflow waves were observed to develop in the regions between low-momentum upwellings and were then drawn into the centre of the vortices. The [15, 60] band does arise and grow between the upwellings, and there is some evidence that it begins to be drawn under the vortices at higher values of Re_z, however it does not exhibit this behaviour to the same degree as the low-speed case, where the travelling wave energy is drawn almost entirely into the upwellings.

These data do not necessarily paint a complete picture of the behaviour of the travelling wave. Owing to the sensitivity of the CTA tuning to transonic effects (Kovasznay 1950), it is possible that the flow velocity in the upwellings is low enough that these effects become important. This would detune the CTA and dramatically lower its frequency response. In this case, the regions dominated by travelling waves may extend further under the upwellings and simply may not be resolved in the low-velocity region. It is also possible that this behaviour occurs, but only downstream of the measurement region. Further study is therefore required to investigate this behaviour further.

The second frequency band of interest is [80, 130] and is depicted in figure 9. The energy in this band is concentrated almost exclusively along the leeward edges of each upwelling. Based on studies of low-speed crossflow (White & Saric 2005; Bonfigli & Kloker 2007) and the expected similarity in the physical mechanisms driving crossflow instability in both Mach regimes, this is the region in which secondary instability is expected to develop. The location of this energy does not change noticeably as Re_z increases.

Figure 10 depicts contours of the normalized r (a) and θ (b) components of $\boldsymbol{\nabla}(\rho u)$ at $Re_z = 3.86 \times 10^6$ computed using fourth-order finite differences. The line contour

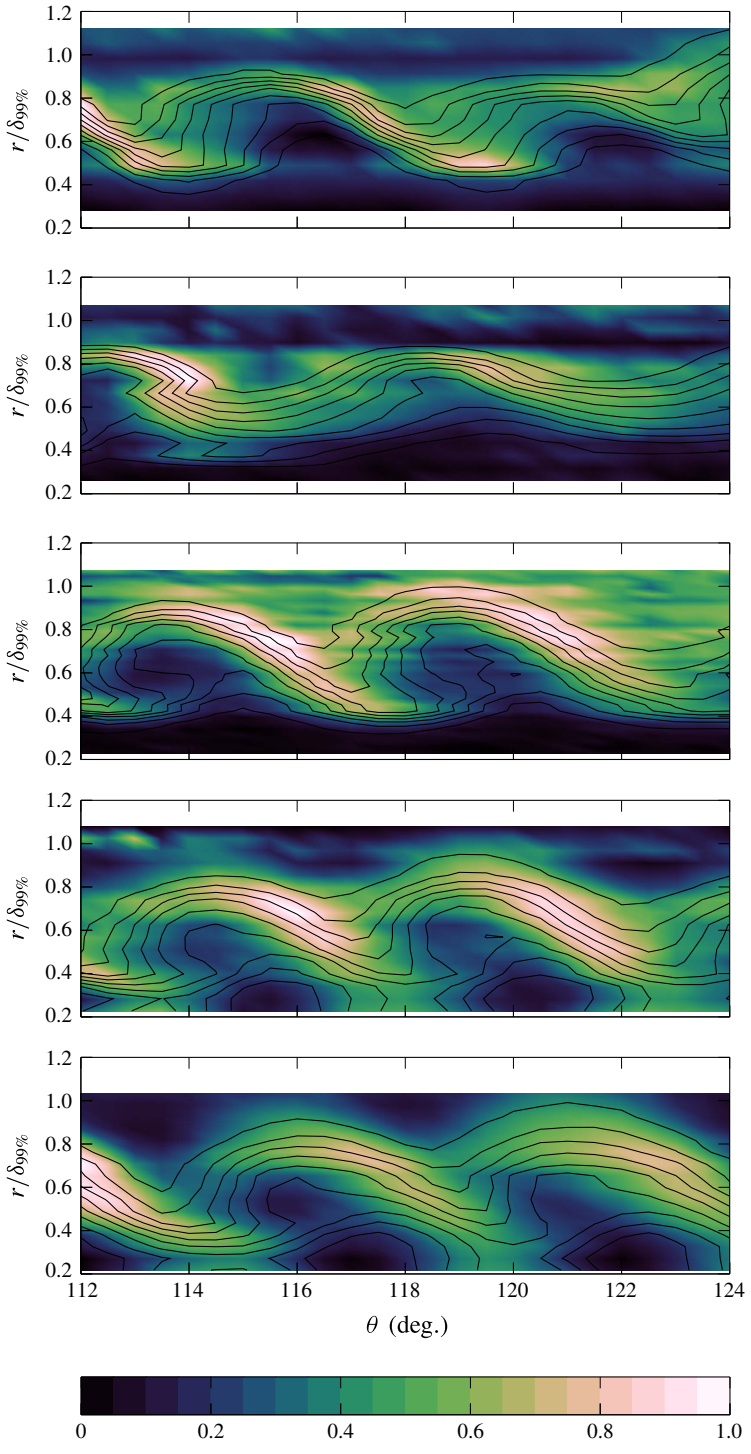

FIGURE 9. (Colour online) Contours of r.m.s. fluctuations in the [80, 130] band. Contour values are of the r.m.s. of the filtered signal normalized by the maximum filtered r.m.s. measured across all measurement stations. Starting from the top, the locations are: $Re_z = 3.5 \times 10^6$, 3.6×10^6, 3.7×10^6, 3.8×10^6 and 3.9×10^6.

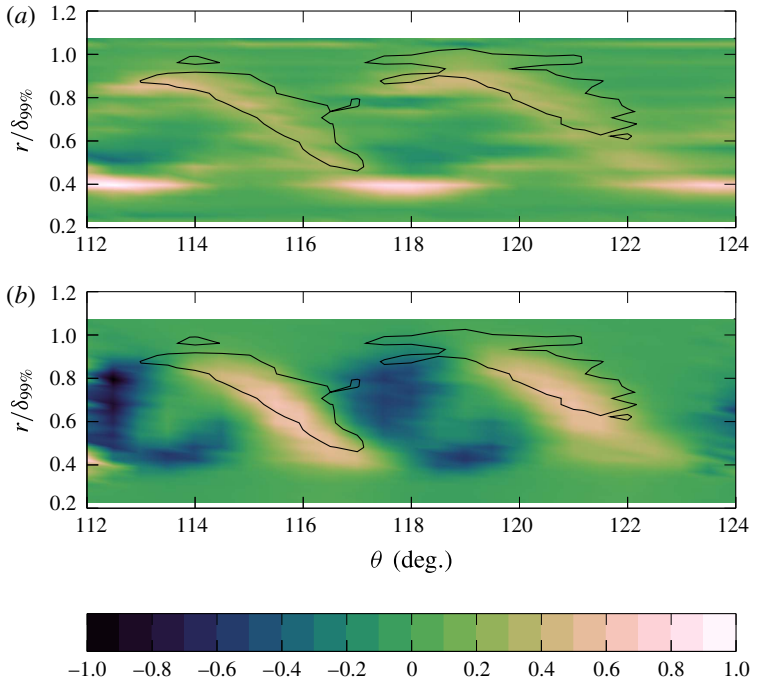

FIGURE 10. (Colour online) r gradient (a) and θ gradient (b) of ρu overlaid with 70 % contour lines of energy in the [80, 130] band at $Re_z = 3.86 \times 10^6$. Colour contours are of the respective gradient normalized by its maximum amplitude (e.g. $\partial_\theta(\overline{\rho u})/|\partial_\theta(\overline{\rho u})|_{max}$).

overlay represents the 70 % contour of energy in the [80, 130] band. The location of the high-energy regions have a one-to-one correspondence with the regions of large positive $\partial(\overline{\rho u})/\partial\theta$ and appear to have no relationship with $\partial(\overline{\rho u})/\partial r$. Further, the high-energy regions extend somewhat over the top of each upwelling beyond the extent of the high $\partial(\overline{\rho u})/\partial\theta$ regions as they are drawn over the top by the stationary vortices.

Additionally, low-speed studies have shown that type-I secondary instabilities occur at frequencies that are proportional to U_e/δ. White & Saric (2005) have shown that the expected frequency should be $f \approx U_e/(2\delta)$. Applying this relationship to U_e based on the run conditions in M6QT and δ based on the above contours, the predicted frequency of a type-I secondary instability is $f \approx 120$ kHz, which falls into the [80, 130]. Together with the location of this signal and the numerical results obtained by Moyes *et al.* (2016), the frequency scaling provides strong evidence that the [80, 130] band represents the signature of an incipient type-I secondary instability. Type-II secondary instability was never observed, as the expected frequency is beyond the useful frequency response of the CTA system.

Three distinct modes have been identified (stationary crossflow, travelling crossflow and type-I secondary instability) and it is instructive to track the growth of each mode individually. Figure 11 depicts the growth of the amplitude of each mode normalized by its amplitude at the most upstream measurement location. These mode amplitudes were defined as the amplitude of the mode shapes for the stationary wave, and the r.m.s. of the corresponding band-passed signal for unsteady modes.

It is an established fact in the low-speed literature that stationary crossflow waves rapidly become nonlinear and saturate, consistent with the present observations. On

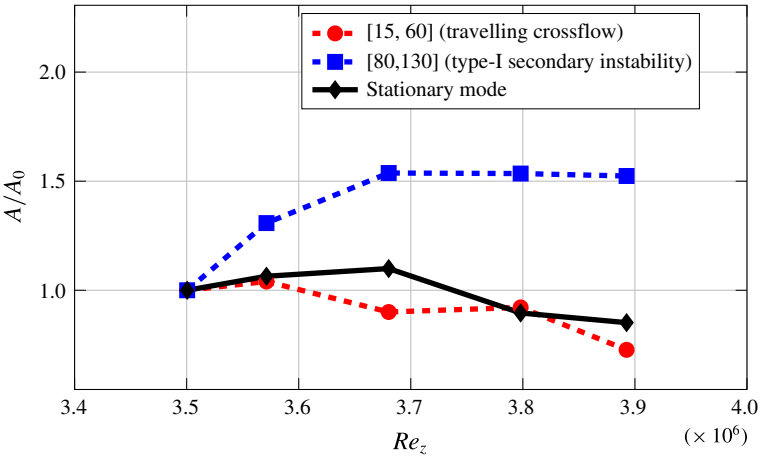

FIGURE 11. (Colour online) Growth of each of the three identified modes.

the contrary, unsteady modes such as the travelling wave and type-I secondary instability have generally been observed to grow. However, the present behaviour is not unprecedented in the low-speed literature. In the experiments performed by White & Saric (2005), while most cases showed the travelling wave to grow monotonically, each case exhibited a temporary decrease in growth rate concurrent with the inception of secondary instability, and the low-forcing case in particular exhibited a brief attenuation of the travelling wave (see figure 18, White & Saric 2005). The same low-forcing case also showed a region of nearly constant amplitude of the type-I secondary instability prior its rapid growth leading to breakdown. It is therefore possible that the region captured in the present study is analogous to this small region just before the explosive growth of the secondary instability in White & Saric (2005).

However, the type-I secondary instability in White & Saric (2005) exists in a region of length $\Delta Re_x \approx 4.8 \times 10^4$ before its rapid growth leading to breakdown. In the present hypersonic case, the type-I secondary instability has been in existence for at least $\Delta Re_z = 4 \times 10^5$, an order of magnitude longer. Given that the IR thermography does not show evidence of breakdown (figure 4), it is likely that the explosive growth leading to breakdown does not occur on the model at all. The base of the model is at $Re_z \approx 4.3 \times 10^6$, extending the range of slow or no growth to $\Delta Re_z \approx 8 \times 10^5$.

This implies that if, like the low-speed case, the type-I secondary instability is ultimately responsible for breakdown, this process occurs nearly an order of magnitude slower (in terms of Reynolds number) in the hypersonic boundary layer. Alternatively, this may be evidence that, while the early time behaviour of hypersonic crossflow appears very similar to the low-speed case, the breakdown mechanisms may differ. As transition to turbulence never occurs on the model, further experimentation is required to address which of these hypotheses are correct.

3.3. *A note on the effect free-stream fluctuations at downstream locations*

It is evident from figure 6 that there is a noticeable increase in the fluctuation levels beginning at the middle measurement location, $Re_z = 3.7 \times 10^6$. Per the discussion presented in § 2.2, the 'noisy' region of the free stream is expected to intersect with

the model further downstream than depicted in figure 3 along the leeward side of the cone. It is thus apparent that this occurs at approximately this middle measurement location depicted in these results.

According to Hofferth & Saric (2012), the free-stream noise is contained primarily in frequency bands in the range $f < 100$ kHz, largely coincident with the travelling wave observed in the present experiment. It is therefore likely that if the free-stream noise has a meaningful effect on the stability of the boundary layer this far downstream, that this would be reflected in the behaviour of the travelling wave, either through simple superposition or through nonlinear interaction.

A bispectral analysis (Hinich & Clay 1968) was performed at each measurement location using the normalization proposed by Hinich & Wolinsky (2005). This analysis produced no evidence of quadratic phase-coupled interactions among the frequencies in this band associated with both the travelling wave and the free-stream fluctuations. In light of this, it is likely that any effect these fluctuations have on the travelling waves would be observed as a simple superposition of the two phenomena. While there is indeed a slight increase in the measured travelling wave amplitude at $Re_z = 3.8 \times 10^6$, it is impossible to ascertain whether this is due to the effect of free-stream noise or a feature of the travelling wave evolution. It is, at any rate, a small effect.

Additionally, the bispectral analysis did not indicate any interaction between the free-stream noise band and either the stationary mode or the secondary instability. Since the free-stream noise band does not coincide with these two modes, there is no other known mechanism by which the free-stream noise can contaminate the measurements of these modes in the absence of nonlinear interactions.

4. Conclusions

This experiment represents the first detailed data taken throughout the boundary layer in a hypersonic, crossflow-dominated flow. Stationary crossflow vortices were observed to dramatically modify the mean flow. Evidence of coexisting travelling crossflow waves was also observed. A high-frequency secondary instability was observed to grow along the leeward edge of the upwellings in the modified mean flow. Transition to turbulence is not observed in the measurement region and IR thermography suggests it never occurs on the model.

The growth of crossflow instability in a Mach 6 boundary layer is remarkably consistent with that at low speeds. The stationary mode is dominant and causes substantial modification to the mean flow before reaching saturation and beginning to attenuate. Its mode shape features a secondary peak that develops as the stationary wave reaches saturation, though this peak appears below the primary peak, in contrast to the low-speed case. Travelling crossflow waves coexist with the stationary wave and occur in the troughs between the low-momentum upwellings. The energy associated with travelling waves is not observed to be drawn into the upwellings, as is the case at low speeds. However further experiments are necessary to determine whether this behaviour is physical or simply due to the limitations of the present experiments.

The observed secondary instability is of the type-I variety. It arises in regions of large positive $\partial(\rho u)/\partial\theta$ along the leeward edge of the upwellings and extends diagonally upward and windward, indicating that the secondary modes are convected up and over the upwellings by the stationary vortices. This behaviour is consistent with low-speed, type-I secondary modes. Contrary to the low-speed observations, however, the type-I secondary instability does not exhibit explosive growth shortly after its inception. Instead, the type-I mode saturates for the remainder of the

measurement region. While this saturation is not unprecedented (White & Saric 2005), the lack of evidence of transition in the IR images give strong support to the idea that no rapid growth and breakdown of the existing type-I mode occurs at any point on the model, even at the base, which represents a 10 % increase in Re_z from the most downstream measurement location.

No type-II secondary instability was observed due to the expected high frequency of such a mode lying outside of the useful range of the CTA system. As a result, it is not possible to address the existence and behaviour of these modes and their relative importance as compared to type-I modes with this data set. Further experiments with modified CTA probes are required to achieve the necessary frequency response to address this issue.

The observed behaviour of the type-I mode may represent an entirely new breakdown mechanism for hypersonic crossflow, or may simply indicate a breakdown process is slower to develop than at low speeds such that the secondary instabilities persist for a sizeable downstream distance before their rapid growth. Answering this question definitively will require additional experimentation. M6QT does not support the use of models larger than the used here. It is therefore unlikely that a complete laminar–turbulent transition of naturally occurring, stationary crossflow waves can be achieved in M6QT. The most likely approach to achieving breakdown in M6QT is therefore through controlled forcing of the most unstable stationary wave. Other existing quiet tunnels can support slightly larger models, but it is unclear whether the additional size is enough to produce a natural transition. Furthermore, these facilities typically do not make off-body measurements, limiting the detail they provide about the structure of the boundary layer.

Acknowledgements

The authors would like to acknowledge the computational contributions of T. Kocian and H. Reed. Funding was provided by NASA and AFOSR through the *National Center for Hypersonic Laminar-Turbulent Transition Research* (AFOSR Grant FA9550-09-1-0341) and by the Texas A&M Foundation through the George Eppright ‘26 Chair in Engineering.

REFERENCES

ADAMS, J. C. JR. 1971 Three-dimensional laminar boundary-layer analysis of upwash patterns and entrained vortex formation on sharp cones at angle of attack. *Tech. Rep.* AEDC-TR-71-215.

BALAKUMAR, P. 2009 Stability of Supersonic Boundary Layers on a Cone at an Angle of Attack. In *39th AIAA Fluid Dynamics Conference, San Antonio, TX, AIAA* 2009-3555.

BALAKUMAR, P. & OWENS, L. R. 2010 Stability of Hypersonic Boundary Layers on a Cone at an Angle of Attack. In *40th AIAA Fluid Dynamics Conference and Exhibit, Chicago, IL, AIAA* 2010-4718.

BIPPES, H. 1999 Basic experiments on transition in three-dimensional boundary layers dominated by crossflow instability. *Prog. Aerosp. Sci.* **35** (4), 363–412.

BLANCHARD, A. E., LACHOWICZ, J. T. & WILKINSON, S. P. 1997 NASA langley Mach 6 quiet wind-tunnel performance. *AIAA J.* **35** (1), 23–28.

BONFIGLI, G. & KLOKER, M. 2007 Secondary instability of crossflow vortices: validation of the stability theory by direct numerical simulation. *J. Fluid Mech.* **583**, 229–272.

BORG, M. P., KIMMEL, R. L. & STANFIELD, S. 2015 Traveling crossflow instability for the HIFiRE-5 Elliptic Cone. *J. Spacecr. Rockets* **52** (3), 664–673.

CHEN, F.-J., WILKINSON, S. P. & BECKWITH, I. E. 1993 Görtler instability and hypersonic quiet nozzle design. *J. Spacecr. Rockets* **30** (2), 170–175.

CHOUDHARI, M. M., CHANG, C.-L., JENTINK, T., LI, F., BERGER, K., CANDLER, G. & KIMMEL, R. 2009 Transition analysis for the HIFiRE-5 vehicle. In *39th AIAA Fluid Dynamics Conference, AIAA* 2009-4056.

DEYHLE, H. & BIPPES, H. 1996 Disturbance growth in an unstable three-dimensional boundary layer and its dependence on environmental conditions. *J. Fluid Mech.* **316**, 73–113.

DOLVIN, D. J. 2008 Hypersonic international flight research and experimentation (HIFiRE). In *15th AIAA International Space Planes and Hypersonic Systems and Technologies Conference, AIAA* 2008-2581.

GOSSE, R., KIMMEL, R. L. & JOHNSON, H. B. 2014 Study of boundary-layer transition on hypersonic international flight research experimentation 5. *J. Spacecr. Rockets* **51** (1), 151–162.

GRONVALL, J. E., JOHNSON, H. B. & CANDLER, G. V. 2012 Hypersonic three-dimensional boundary layer transition on a cone at angle of attack. In *42nd AIAA Fluid Dynamic Conference, New Orleans, LA, AIAA* 2012-2822.

HINICH, M. J. & CLAY, C. S. 1968 The application of the discrete Fourier transform in the estimation of power spectra, coherence, and bispectra of geophysical data. *Rev. Geophys.* **6** (3), 347.

HINICH, M. J. & WOLINSKY, M. 2005 Normalizing bispectra. *J. Stat. Planning Inference* **130**, 405–411.

HOFFERTH, J. W. 2013 Boundary-layer stability and transition on a flared cone in a Mach 6 quiet wind tunnel. Doctoral dissertation, Texas A&M University.

HOFFERTH, J. W., BOWERSOX, R. D. W. & SARIC, W. S. 2010 The Mach 6 quiet tunnel at Texas A&M: quiet flow performance. In *27th AIAA Aerodynamic Measurement Technology and Ground Testing Conference, Chicago, IL, AIAA* 2010-4794.

HOFFERTH, J. W., HUMBLE, R. A., FLORYAN, D. C. & SARIC, W. S. 2013 High-bandwidth optical measurements of the second-mode instability in a Mach 6 quiet tunnel. In *51st AIAA Aerospace Sciences Meeting, Grapevine, TX, AIAA* 2013-0378.

HOFFERTH, J. W. & SARIC, W. S. 2012 Boundary-layer transition on a flared cone in the Texas A&M Mach 6 quiet tunnel. In *50th AIAA Aerospace Sciences Meeting, Nashville, TN, AIAA* 2012-0923.

JULIANO, T. J., BORG, M. P. & SCHNEIDER, S. P. 2015 Quiet tunnel measurements of HIFiRE-5 boundary-layer transition. *AIAA J.* **53** (4), 832–846.

KOHAMA, Y. 1987 Some expectation on the mechanism of cross-flow instability in a swept wing flow. *Acta Mechanica* **66** (1–4), 21–38.

KOHAMA, Y., SARIC, W. S. & HOOS, J. A. 1991 A high-frequency, secondary instability of crossflow vortices that leads to transition. In *Proceedings of Royal Aero. Soc. Conf. on Boundary-Layer Transition and Control*, Cambridge University, pp. 4.1–4.13.

KOVASZNAY, L. S. G. 1950 The hot-wire anemometer in supersonic flow. *J. Aero. Sci.* **17** (9), 565–572.

VAN DEN KROONENBERG, A., RADESPIEL, R., CANDLER, G. V. & ESTORF, M. 2010 Infrared measurements of boundary-layer transition on an inclined cone at Mach 6, In *48th AIAA Aerospace Sciences Meeting, Orlando, FL, AIAA* 2010-1063.

KUEHL, J. J., PEREZ, E. & REED, H. L. 2012 JoKHeR: NPSE Simulations of Hypersonic Crossflow Instability. In *50th AIAA Aerospace Sciences Meeting, Nashville, TN, AIAA* 2012-0921.

LI, F., CHOUDHARI, M. M., CHANG, C.-L., WHITE, J., KIMMEL, R. L., ADAMCZAK, D., BORG, M. P., STANFIELD, S. A. & SMITH, M. 2012 Stability analysis for HIFiRE experiments. In *42nd AIAA Fluid Dynamics Conference, AIAA* 2012-2961.

MACK, L. M. 1984 Boundary-Layer linear stability theory, *AGARD Report No. 709*.

MALIK, M. R., LI, F. & CHANG, C.-L. 1996 Nonlinear crossflow disturbances and secondary instabilities in swept-wing boundary layers. In *IUTAM Symposium on Nonlinear Instability and Transition in Three-Dimensional Boundary Layers* (ed. P. W. Hall & P. W. Duck), pp. 257–266. Springer.

MALIK, M. R., LI, F., CHOUDHARI, M. M. & CHANG, C.-L. 1999 Secondary instability of crossflow vortices and swept-wing boundary-layer transition. *J. Fluid Mech.* **399**, 85–115.

MOYES, A., PAREDES, P., KOCIAN, T. S. & REED, H. L. 2016 Secondary Instability Analysis of Crossflow on a Hypersonic Yawed Straight Circular Cone. In *54th AIAA Aerospace Sciences Meeting, AIAA* 2016-0848.

MUÑOZ, F., HEITMANN, D. & RADESPIEL, R. 2014 Instability modes in boundary layers of an inclined cone at Mach 6. *J. Spacecr. Rockets* **51** (2), 442–454.

OLIVIERO, N. B., KOCIAN, T. S., MOYES, A. J. & REED, H. L. 2015 EPIC: NPSE Analysis of Hypersonic Crossflow Instability. In *45th AIAA Fluid Dynamics Conference, AIAA* 2015-2772.

PARZIALE, N. J., SHEPHERD, J. E. & HORNUNG, H. G. 2013 Differential interferometric measurement of instability in a hypervelocity boundary layer. *AIAA J.* **51** (3), 750–754.

PARZIALE, N. J., SHEPHERD, J. E. & HORNUNG, H. G. 2015 Observations of hypervelocity boundary-layer instability. *J. Fluid Mech.* **781**, 87–112.

PEREZ, E., REED, H. L. & KUEHL, J. J. 2013 Instabilities on a hypersonic yawed straight cone. In *43rd AIAA Fluid Dynamics Conference, San Diego, CA, AIAA* 2013-2879.

REED, H. L. & SARIC, W. S. 1989 Stability of three-dimensional boundary layers. *Annu. Rev. Fluid Mech.* **21** (1), 235–284.

SARIC, W. S., REED, H. L. & WHITE, E. B. 2003 Stability and transition of three-dimensional boundary layers. *Annu. Rev. Fluid Mech.* **35** (1), 413–440.

SCHMISSEUR, J. D., YOUNG, J. O. & SCHNEIDER, S. P. 1996 Measurements of boundary-layer transition on the flat sidewall of a rectangular Mach 4 quiet-flow nozzle. In *34th Aerospace Sciences Meeting and Exhibit, AIAA* 96-0852.

SCHUELE, C. Y., CORKE, T. C. & MATLIS, E. H. 2013 Control of stationary cross-flow modes in a Mach 3.5 boundary layer using patterned passive and active roughness. *J. Fluid Mech.* **718**, 5–38.

SEMPER, M. T. 2013 Examining a hypersonic turbulent boundary layer at low Reynolds number. Doctoral dissertation, Texas A&M University.

SMITS, A. J., HAYAKAWA, K. & MUCK, K. C. 1983 Constant temperature hot-wire anemometer practice in supersonic flows - part 1: the normal wire. *Exp. Fluids* **1** (2), 83–92.

STETSON, K. F. 1982 Mach 6 experiments of transition on a cone at angle of attack. *J. Spacecr. Rockets* **19** (5), 397–403.

SWANSON, E. O. & SCHNEIDER, S. P. 2010 Boundary-Layer Transition on Cones at Angle of Attack in a Mach-6 Quiet Tunnel. In *49th AIAA Aerospace Sciences Meeting, Orlando, FL, AIAA* 2010-1062.

WARD, C. A. C., HENDERSON, R. O. & SCHNEIDER, S. P. 2015 Possible Secondary Instability of Stationary Crossflow Vortices on an Inclined Cone at Mach 6. In *45th AIAA Fluid Dynamics Conference, Dallas, TX, AIAA* 2015-2773.

WASSERMANN, P. & KLOKER, M. 2002 Mechanisms and passive control of crossflow-vortex-induced transition in a three-dimensional boundary layer. *J. Fluid Mech.* **456**, 49–84.

WELCH, P. D. 1967 The use of fast fourier transform for the estimation of power spectra: A method based on time averaging over short, modified periodograms. *IEEE Trans. Audio Electroacoust.* **15** (2), 70–73.

WHITE, E. B. & SARIC, W. S. 2005 Secondary instability of crossflow vortices. *J. Fluid Mech.* **525**, 275–308.